JPL D-1000788

Surface Biology and Geology (SBG)
Observing Terrestrial Thermal Emission Radiometer (OTTER)

Level 3 Surface Mineralogy Algorithm Theoretical Basis Document (ATBD)

Version 0.5
November 7, 2023

Michael S. Ramsey
SBG-TIR Algorithm Development Team
University of Pittsburgh

James O. Thompson
SBG-TIR Algorithm Development Team
University of Texas, Austin

JPL D-1000788

National Aeronautics and
Space Administration

Jet Propulsion Laboratory
4800 Oak Grove Drive
Pasadena, California 91109-8099
California Institute of Technology

This research was carried out at the Jet Propulsion Laboratory, California Institute of Technology, under a contract with the National Aeronautics and Space Administration.

Change History Log

Revision	Effective Date	Prepared by	Description of Changes
Draft	08/22/2023	Michael Ramsey	First draft outline
V0.5	09/24/2023	Michael Ramsey	Addition of text and editing
	09/27/2023	James Thompson	Addition of text and editing
	10/01/2023	Michael Ramsey	Editing
	11/07/2023	Micheal Ramsey	Clean up prior to peer review

Contacts

Readers seeking additional information about this study may contact the following:

Michael S. Ramsey
University of Pittsburgh
4107 O'Hara Street, Room 509
Pittsburgh, PA 15260-3332
Email: mramsey@pitt.edu
Office: 1-412-624-8772

James O. Thompson
University of Texas, Austin
10611 Exploration Way
Austin, TX 78758
Email: james.thompson@beg.utexas.edu
Office: 1-512-471-6775

SBG Science Team

Team members:

Abstract

The 2017-2027 Decadal Survey for Earth Science and Applications from Space (ESAS 2017) was released in January 2018. ESAS 2017 was driven by input from the scientific community and policy experts and provides a strategic vision for the next decade of Earth observation that informs federal agencies responsible for the planning and execution of civilian space-based Earth-system programs in the coming decade. These include the National Aeronautics and Space Administration (NASA), the National Oceanic and Atmospheric Administration (NOAA), and the U.S. Geological Survey (USGS). NASA has, thus far, utilized this document as a guide to inform exploration of new Earth mission concepts that are later considered as candidates for fully funded missions. High-priority emphasis areas and targeted observables include global-scale Earth science questions related to hydrology, ecosystems, weather, climate, and solid earth. One of the Designated Observables (DO's) identified by ESAS 2017 was Surface Biology and Geology (SBG) with a goal to acquire concurrent global hyperspectral visible to shortwave infrared (VSWIR; 380–2500 nm) and multispectral mid-wave and thermal infrared (MWIR: 3–5 μm; TIR: 8–12 μm) image data at high spatial resolution (~30 m in the VSWIR and ~ 60 m in the TIR) at sub-monthly temporal resolution globally. The final sensor characteristics will be determined during the mission formulation phase, but ESAS 2017 provides guidance for a VSWIR instrument with 30–45 m pixel resolution, ≤16 day global revisit, SNR > 400 in the VNIR, SNR > 250 in the SWIR, and 10 nm sampling in the range 380–2500 nm. It also recommends a TIR instrument with more than five channels in 8–12 μm, and at least one channel at 4 μm, ≤60 m pixel resolution, ≤3 day global revisit, and noise equivalent delta temperature (NEdT) ≤0.2 K (NASEM, 2019; Schimel and Poulter, 2020). Alone, SBG will provide a comprehensive global monitoring for multiple scientific disciplines. Complemented with systems like Landsat and Sentinel-2 VSWIR, global change processes with faster than 16-day global change rates can be mapped. Further, complimented with planned TIR systems such as LSTM and TRISHNA, the temporal revisit could be as frequent as 1-day at the equator, making the system excellent for tracking dynamic thermal features and hazards. This document describes the planned Level-3 Surface Mineralogy (SM) product for the SBG TIR data.

Contents

Figures

Tables

1 Introduction

The Surface Biology and Geology (SBG) thermal infrared (TIR) instrument – termed the Observing Terrestrial Thermal Emission Radiometer (OTTER) consists of a TIR multispectral scanner with six spectral bands operating between 8.0 and 13.0 µm and two mid-infrared (MIR) bands between 3.0 and 5.0 µm, with a 60 m pixel resolution, an equatorial three day revisit, and a noise equivalent delta temperature (NEdT) ≤0.2 K (NASEM, 2019; Schimel and Poulter, 2020). The TIR data will be acquired with a wide swath width of 935 km (60°) from an altitude of ~700 km. OTTER instrument design and data derive their heritage from the ECOSTRESS instrument, which is a five-channel multispectral TIR scanner that was launched to the International Space Station (ISS) in June 2018. ECOSTRESS has a 70-m spatial resolution with a wide swath width and revisit time that is variable between 3-5 days on average (Table 1).

Table 1: SBG measurement characteristics compared to other operational and planned (*) spaceborne TIR instruments

Instrument	Platform	Resolution (m)	Revisit (days)	Daytime overpass	TIR bands (8-12.5 µm)	Launch year
OTTER	SBG	60	3	12:30	6	2028*
ECOSTRESS	ISS	38 × 68	3-5	Variable	5	2018
LSTM		50	4	13:00	5	2028*
TRISHNA		57	2-3	13:00	4	2025*
ASTER	Terra	90	16	10:30	5	1999
ETM+/TIRS	Landsat 7/8	60-100	16	10:11	1/2	1999/2013
VIIRS	Suomi-NPP	750	Daily	1:30 / 13:30	4	2011
MODIS	Terra/Aqua	1000	Daily	10:30 / 13:30	3	1999/2002

GOES	Multiple	4000	Daily	Every 15 min	2	2000

This document outlines the theory and methodology for generating the OTTER Level-3 (L3) surface mineralogy (SM) product. The SM product uses the L2 TIR surface emissivity data as input together with a spectral library of the most common Earth surface minerals acquired in emission in the laboratory at 2 cm^{-1} resolution (Christensen et al., 2000). Most silicates, carbonates, and other rock-forming minerals have diagnostic spectral features in the TIR regions characterized by the strongest absorption bands also known as Reststrahlen features (Figure 1). The SM algorithm uses the principal of linear spectral mixing in TIR region where the larger absorption coefficients typical of most rock-forming minerals limit photon transmission and scattering within the mineral grains. The emitted spectrum, therefore, has spectral features in linear proportion to the areal abundance of those minerals in the unknown sample (Ramsey and Christensen, 1998). In contrast, this scattering is more prevalent in the visible short-wave infrared (VSWIR) causing non-linearity in the reflectance spectrum and requiring more complex mapping approaches to mineral identification (Clark et al., 2003, Connelly et al., 2021).

The SM product is applied to the at-surface TIR emissivity data derived from the L2 land surface temperature and emissivity (LSTE) product. It will be applied to a limited subset of OTTER data determined using a seasonally adjusted global emissivity mask (e.g., Hulley et al., 2015). Only OTTER data with an average emissivity of < 0.92 (avoiding significant vegetation cover) and an average temperature > 0 C (avoiding snow and ice), which corresponds to ~ 30% of the Earth's land surface, will be mapped using the SM algorithm. The emission spectrum from any pixel meeting these criteria is modeled using the pre-determined spectral library as input and producing a best-fit suite of mineral endmember images plus their corresponding residual error

images. A root-mean-squared (RMS) error image is also produced to assess the overall goodness-of-fit of the model. Finally, a weight percent silica (WPS) image is also produced using the approach of Hook et al. (2005).

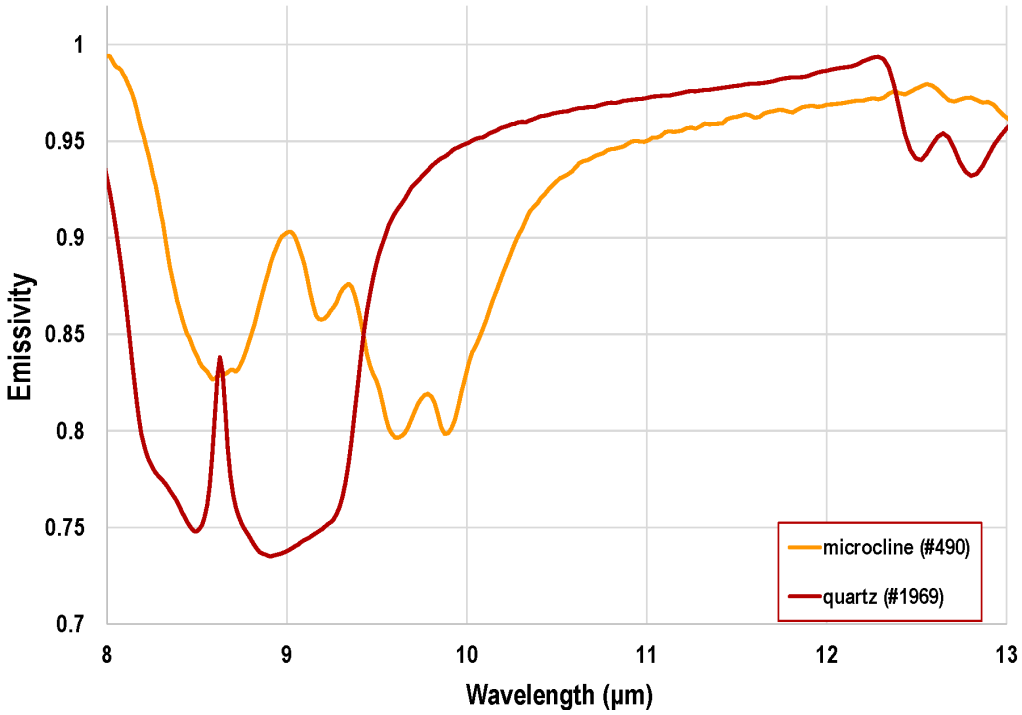

Figure 1: TIR (8.0 – 13.0 µm) spectral emissivity of quartz and microcline (potassium feldspar) showing the diagnostic Reststrahlen emissivity features for both minerals. The inclusion of a sixth TIR band at ~ 10.3 mm allows better discrimination of these primary rock-forming minerals using the SM algorithm. Data from: ASU Spectral Library (Christensen et al., 2000).

The SM data will be assessed and validated throughout the mission using pseudo-invariant sand dune sites in the Western United States, Africa, and China (Hulley and Baldridge, 2013; Helder et al., 2010). Sand dunes present ideal calibration sites for TIR emissivity-based compositional studies because they have well-mixed, unimodal surfaces with low percentages of vegetation and shadows (Ramsey et al., 1999; Scheidt and Ramsey, 2010; Scheidt et al., 2011).

The remainder of the document will discuss the SBG instrument characteristics, provide a background on TIR remote sensing, give a full description and background on the SM algorithm, provide quality assessment, discuss numerical simulation studies and, finally, outline a validation plan.

2 SBG Instrument Characteristics

2.1 Band positions

The TIR instrument will acquire data from a sun-synchronous orbit of ~700 km with 60m spatial resolution in eight spectral bands with two of those located in the MIR and six in the TIR region of the electromagnetic spectrum between 3 and 13 μm (Figure 2). The center position and width of each band is provided in Table 2. The positions of the first three TIR bands closely match those of the ASTER sensor (ASTER bands 10 – 12), whereas the longest two TIR bands match those of the MODIS sensor (MODIS bands 31-32), which are typically used for "split-window" type temperature applications (Brown and Minnett 1999; Coll and Caselles 1997; Prata 1994; Price 1984; Wan and Dozier 1996; Yu et al. 2008). The OTTER band centered at 10.3 μm was added early in Phase A in order to more accurately detect surface mineralogy (e.g., distinguishing between silicate feldspars and quartz) as well as sulfate aerosols conversion in volcanic plumes (Figure 3). The two MIR bands are present to detect a larger range of high surface temperatures (Table 2) without saturating (e.g., 500 – 1200 K) as well as the potential of elevated CO_2 emission sources using the 4.8 μm band.

It is expected that small adjustments to the band positions, widths, and transmission will be made based on ongoing engineering filter performance capabilities and finalized once the filters are fabricated.

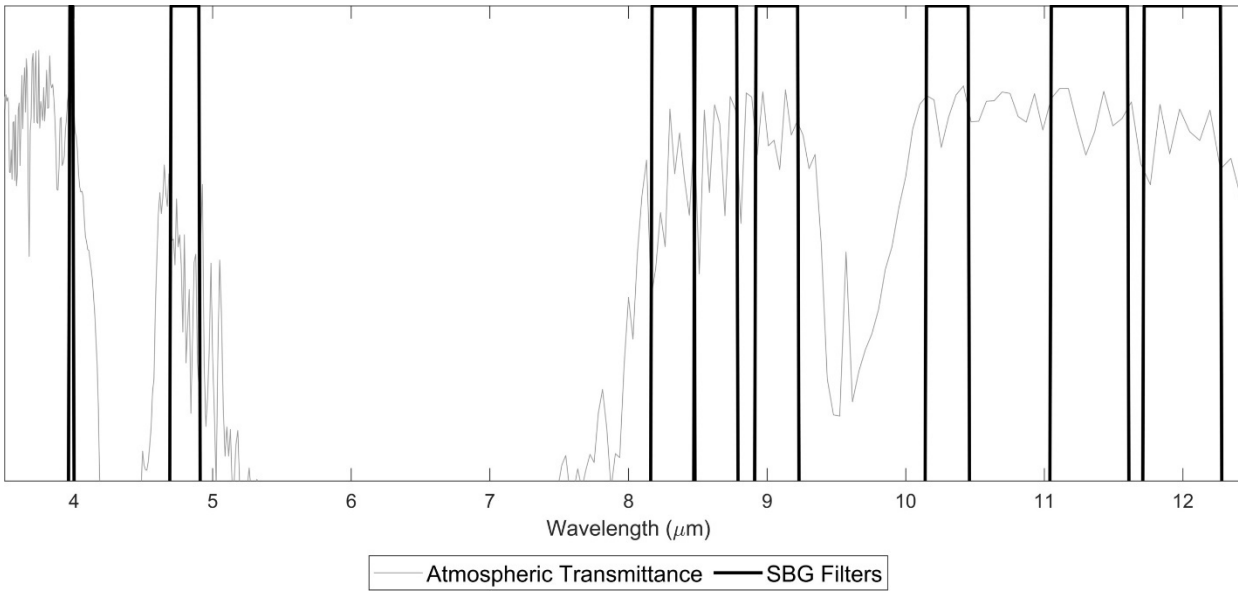

Figure 2: SBG boxcar filters for two MIR bands and six TIR bands from 3.8-12.5 microns with a typical atmospheric transmittance spectrum in gray highlighting the atmospheric window regions. Note the spectral width and position of the filters are nearly finalized (see Table 2), however the spectral shape will be determined after the detectors are fabricated.

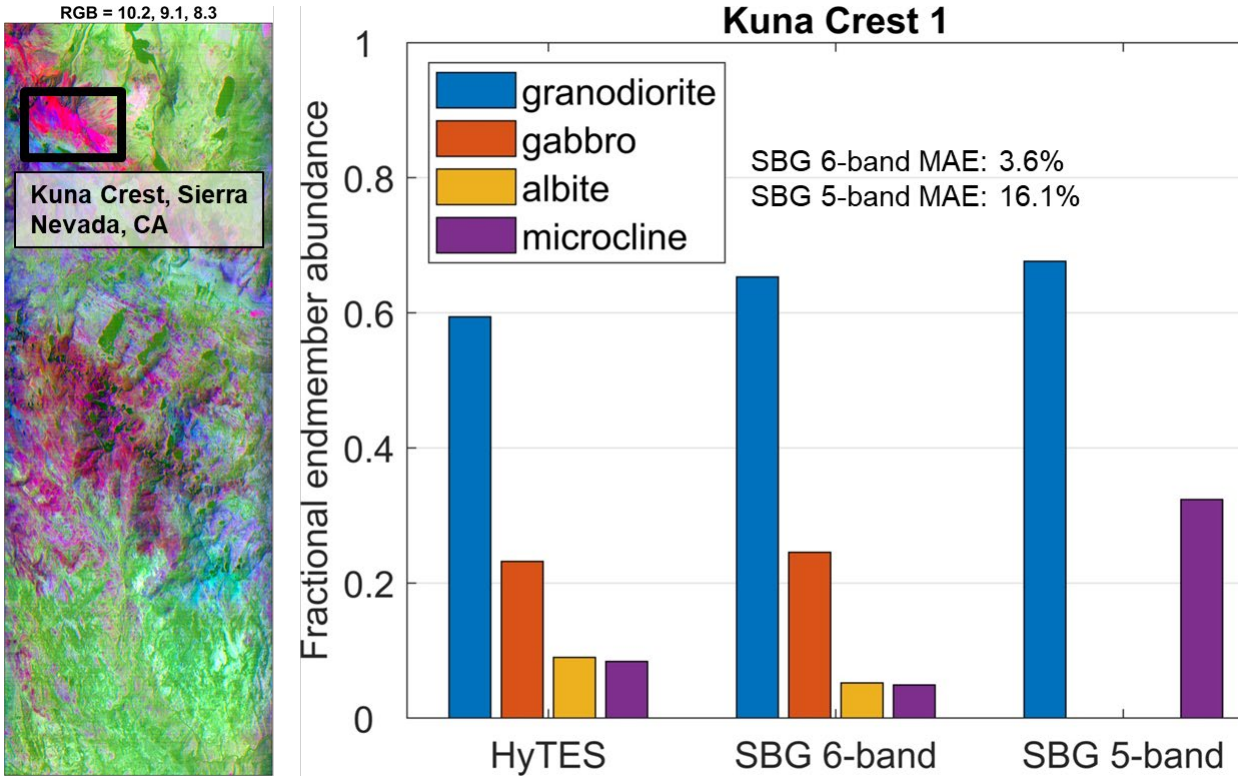

Figure 3: Benefits of these additional bands include improved sensitivity in discriminating different rock types, for example in this case in Sierra Nevada Mountains we can discriminate felsic and mafic minerals and have a result similar to that of HyTES, a hyperspectral TIR sensors.

2.2 Radiometer

The TIR instrument will operate as a push-whisk mapper very similar to ECOSTRESS with 256 pixels in the cross-whisk direction for each spectral channel. As the spacecraft moves forward, the scan mirror sweeps the focal plane image 68.8° across nadir in the cross-track direction, which enables a wide swath (935 km) from the spacecraft altitude of ~700 km. Each sweep is 256-pixels wide with the different spectral bands are swept across a given point on the ground sequentially. The scan mirror rotates at a constant angular speed and images two on-board blackbody targets at 300 K and 340 K with each cross-track sweep every 1.29 seconds to provide gain and offset calibrations.

Table 2: SBG band positions and characteristics

Band #	Center Wavelength (µm)	Spectral Width (FWHM) (nm)	Tolerance Center Wavelength (± nm)	Tolerance Spectral Width (±nm)	Knowledge Center Wavelength (±nm)	Knowledge Spectral Width (±nm)	Accuracy (Kelvin)	NEΔT (K)	Range (K)
MIR-1	3.98	20	50	10	10	10	≤3@750	≤0.3@750	700-1200
MIR-2	4.8	150	100	50	20	20	≤1@450	≤0.2@450	400-800
TIR-1	8.32	300	100	50	20	20	≤0.5@275	≤0.2@275	200-500
TIR-2	8.63	300	100	50	20	20	≤0.5@275	≤0.2@275	200-500
TIR-3	9.07	300	100	50	20	20	≤0.5@275	≤0.2@275	200-500
TIR-4	10.30	300	50	50	20	20	≤0.5@275	≤0.2@275	200-500
TIR-5	11.35	500	100	50	20	20	≤0.5@275	≤0.2@275	200-500
TIR-6	12.05	500	100	50	20	20	≤0.5@275	≤0.2@275	200-500

Table 3: SBG TIR instrument and measurement characteristics

Spectral	
Bands (µm)	3.95, 4.8, 8.32, 8.63, 9.07, 10.3, 11.35, 12.05
Bandwidth (nm)	20, 150, 300, 300, 300, 300, 500, 500
Accuracy at 300 K	<0.01 µm
Radiometric	
Range	TIR (8-12.5 µm) bands (200 - 500 K) MIR 4.8 µm band (400 - 800 K) MIR 3.95 µm band (700 -1200 K)
Resolution	< 0.05 K, linear quantization to 14 bits
Accuracy	< 0.5 K 3-sigma at 275 K
Precision (NEdT)	< 0.2 K
Linearity	> 99% characterized to 0.1 %
Spatial	
IFOV	60m
MTF	> 0.65 at FNy
Scan Type	Push-Whisk
Swath Width at 665-km altitude	935 km (± 34.4°)
Cross Track Samples	10,000 *(check)*
Swath Length	10,000 *(check)*
Down Track Samples	256
Band to Band Co-Registration	0.2 pixels (12 m)
Pointing Knowledge	10 arcsec (0.5 pixels)
Temporal	
Orbit Crossing	Multiple
Global Land Repeat	Multiple
On Orbit Calibration	
Lunar views	1 per month {radiometric}
Blackbody views	1 per scan {radiometric}
Deep Space views	1 per scan {radiometric}
Surface Cal Experiments	2 (day/night) every 5 days {radiometric}
Spectral Surface Cal Experiments	1 per year
Data Collection	
Time Coverage	Day and Night
Land Coverage	Land surface above sea level
Water Coverage	n/a
Open Ocean	n/a
Compression	2:1 lossless

3 Theory

3.1 Mid-wave and Thermal Infrared Remote Sensing Background

The at-sensor measured radiance in the infrared region (3–13 μm) consists of a combination of different terms from surface emission, solar reflection, and atmospheric emission and attenuation. The Earth-emitted radiance is a function of the temperature and emissivity of the surface, which is then attenuated by the atmosphere on its path to the satellite. The emissivity of an isothermal, homogeneous emitter is defined as the ratio of the actual emitted radiance to the radiance emitted from a blackbody (Figure 1) at the same thermodynamic temperature (Norman and Becker 1995), $\epsilon_\lambda = R_\lambda / B_\lambda$. Emissivity is an intrinsic property of the surface material and is an independent measurement from the surface temperature, which varies with irradiance, local atmospheric conditions, time of day, and specific conditions causing elevated temperature (e.g., wildfires, volcanic eruptions, etc.). The emissivity of most natural Earth surfaces varies from ~0.7 to close to 1.0, for the TIR wavelength (8–13 μm) for spatial scales <100 m. Narrowband emissivities less than 0.85 are typical for most desert and semi-arid areas due to the strong quartz absorption feature (Reststrahlen band) between the 8.0 and 9.5 μm, whereas the emissivity of green vegetation and water are generally greater than 0.95 and spectrally flat in the TIR. Dry and senesced vegetation as well as ice and snow can have lower emissivity values in the wavelengths longer than 10 μm.

The atmosphere also emits TIR radiation, a percentage of which reaches the sensor directly as "path radiance," whereas some amount is radiated downward to the surface (irradiance) and reflected back to the sensor. This is commonly known as the reflected downwelling sky irradiance. One effect of the sky irradiance is the reduction of the spectral contrast of the emitted surface radiance, due to Kirchhoff's law. Assuming the spectral variation in emissivity is small

(Lambertian assumption) and using Kirchhoff's law to express the hemispherical-directional reflectance as directional emissivity ($\rho\lambda=1-\epsilon\lambda$), the at-sensor measured radiance in the infrared spectral region is a combination of three primary terms: the Earth-emitted radiance, reflected downwelling radiance (thermal + solar components), and total atmospheric path radiance (thermal + solar components).

$$L_{obs}(\lambda,\theta) = \tau_\lambda(\theta)\left[\epsilon_\lambda B(\lambda,T_s) + \rho_\lambda\left(L_s^{\downarrow}(\lambda,\theta) + L_t^{\downarrow}(\lambda,\theta)\right)\right] + L_t^{\uparrow}(\lambda,\theta) + +L_s^{\uparrow}(\lambda,\theta) \quad (1)$$

where: $L(\lambda,\theta)$ = at-sensor radiance, λ is wavelength, θ is the satellite viewing angle, $\epsilon\lambda$ is the surface emissivity, $\rho\lambda$ is surface reflectance, $B(\lambda,T_s)$ is the Planck function describing radiance emitted at surface temperature, T_s, $L_s^{\downarrow}$ is the total (diffuse and direct) downwelling solar radiance, $L_t^{\downarrow}$ is the downwelling thermal irradiance, $\tau\lambda$ (θ) is the atmospheric transmittance, $L_s^{\uparrow}$ (λ,θ) is the upward path solar radiance, and $L_t^{\uparrow}$ (λ,θ) is the upward thermal path radiance reaching the sensor.

The Temperature Emissivity Separation (TES) Algorithm originally created for ASTER TIR (Gillespie et al., 1998) data will be used to derive surface temperature and emissivity from the OTTER radiance data. The algorithm combines and improves upon some core features from previous temperature emissivity separation algorithms. TES combines the normalized emissivity method (NEM), the ratio, and the minimum-maximum difference (MMD) algorithm to retrieve temperature and a full emissivity spectrum. The NEM algorithm is used to estimate temperature and iteratively remove the sky irradiance, from which an emissivity spectrum is calculated, and then ratioed to their mean value in the ratio algorithm. At this point, only the shape of the emissivity spectrum is preserved, but not the amplitude. In order to compute an accurate temperature, the correct amplitude is then found by relating the minimum emissivity to the spectral contrast (MMD). Once the correct emissivity values are found, a final temperature can be calculated with the maximum emissivity value. Additional improvements involve a refinement of ϵ_{max} in the

NEM module and refining the correction for sky irradiance using the ε_{min}-MMD final emissivity and temperature values. Numerical modeling studies showed that TES can recover temperatures to within 1.5 K and emissivity values to within 0.015 over most scenes, assuming well calibrated, accurate radiometric measurements with a minimum of noise (Gillespie et al. 1998).

3.2 Compositional Detection in the TIR

The emission spectra from laboratory samples or pixels in a TIR image that are comprised of more than one mineral reflect those mineral endmembers by a combination of their characteristic spectral features. Perhaps more importantly, under most circumstances, those features are a linear combination of the areal percentage of the mineral endmembers themselves (Figure 4). The assumption of linear mixing of thermal radiant energy is valid due to the fact that most geologically significant minerals have very high absorption coefficients in the TIR, resulting in a much shorter path length and less scattering for the emitted photons. As a result, the majority of the energy detected by a sensor has interacted with only one surface particle (Ramsey and Christensen, 1998, *REFS*).

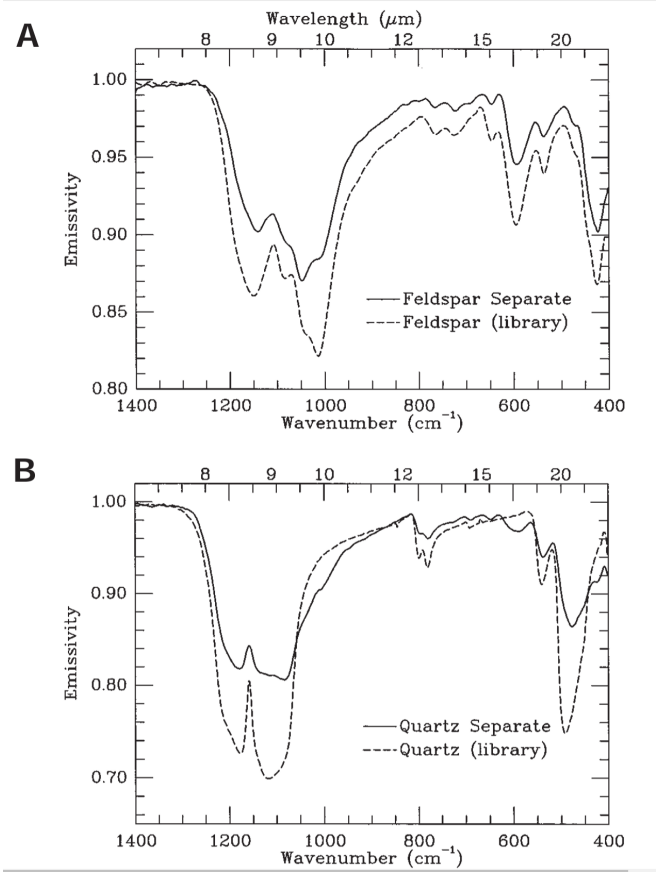

Figure 4: Emission spectra of the best-case separation of feldspar and quartz derived from the heavy-liquid technique. (A) Feldspar. (B) Quartz. Each spectrum is plotted with a pure library end member for comparison. From Ramsey and Christensen (1998).

Upon mixing, the spectral features from surface particles are retained in proportion to their areal extent. For example, Ramsey and Christensen (1998) showed this in spectra from Kelso Dunes, CA. The individual mineral grains in sand samples were separated using a heavy liquid technique, which proved to be only partially successful (Figure 4). Contamination of each spectrum by the other mineral is visible in the spectral features being most evident in the quartz spectrum, where 34% feldspar still remained. This contamination shows as a reduction in contrast of the primary absorption band at 1150 cm^{-1}, the development of band shoulder at 1000 cm^{-1}, and several smaller absorption bands between 600 cm^{-1} and 700 cm^{-1}.

3.2.1 Spectral Mixture Analysis (SMA)

This allows for a relatively straight forward approach to spectral analysis using some variation of linear spectral mixture analysis (Heinz 2001; Somers et al. 2011; Tompkins et al. 1997). This can be summarized by equation 2.

$$\varepsilon(\lambda)_{mix} = \sum_{i=1}^{\eta}(\zeta_i \cdot \varepsilon(\lambda)_i) + \delta(\lambda); \quad \langle 1 \rangle \quad \sum_{i=1}^{\eta} \zeta_i = 1.0\,; \quad \langle 2 \rangle \quad \zeta_i \geq 0 \qquad (2)$$

Where, η is the number of endmembers modeled, ζ_i is the areal fraction of the i^{th} endmember's emissivity ($\varepsilon(\lambda)_i$) and $\delta(\lambda)$ is the residual difference between the measured and modeled emissivity at wavelength (λ). The first constraint $\langle 1 \rangle$ placed upon the system is that the endmember fractions must sum to 1.0 (100%) per pixel for each model run. Because the equation is a relatively simple constrained, least-squares fit, negative endmember fractions are mathematically valid and occur in the rare cases where the spectrum of the unknown sample has a lower emissivity in some/all of the spectral range versus that of the endmember spectra. In these cases, the second constraint $\langle 2 \rangle$ is tested and negative endmembers removed from the modeling.

Therefore, assuming that the pure mineral spectra (i.e., the endmembers) are known, TIR spectra can be linearly deconvolved using the least-squares approach (equation 2) to ascertain the mineralogic percentages. For image-based analyses, this results in one image per endmember together with several checks on the accuracy of that model fit. A residual error image is produced for each TIR band, which is simply the measured – the modeled emissivity in that spectral band. Areas of high residual error indicate a poor model fit in that spectral band with the chosen endmembers. This difference is a critical measure of the retrieval algorithm's fit, and easily visualized where displayed versus wavelength, or as an image in the case of remotely gathered data (Gillespie et al., 1990). High residual errors at specific wavelengths indicate the possibility of an unmodeled absorption feature not present in either the endmember or mixture spectrum. An examination of residuals may also reveal nonlinear behavior at certain wavelengths as well as highlight areas of poor atmospheric correction and/or low instrument signal to noise (SNR).

A singular goodness-of-fit error image is also produced for each image/model run. The root-mean-squared (RMS) error image becomes invaluable in order to assess the overall quality of

a given algorithm iteration. For an instrument with (m) wavelength bands, the RMS is related to the per-band residual error (δ(λ)) using equation 3.

$$RMS = \sqrt{\frac{\left(\sum_{j=1}^{m} \delta(\lambda)_j^2\right)}{m}} \quad (3)$$

In the most common approach to spectral deconvolution, the number of endmembers modeled must be ≤ the number of spectral bands. Thus, for hyperspectral data, the number of possible endmembers can be quite high (to the point of being geologically implausible). However, for multispectral data, the limited number of spectral bands commonly places a tight constraint on the number of endmembers. This constraint may be acceptable if one is modeling the highest percentage two or three mineral endmembers using five or six band TIR data. If more than five or six endmember are present (or if one wants to test for the presence of many unknown minerals), a different approach is required such as the Multiple Endmember SMA (MESMA), which uses a combinatorial approach to testing all possible endmember combinations for the one producing the best fit (e.g., the lowest RMS error).

3.2.2 Multiple Endmember SMA (MESMA)

Linear SMA assumes that a mixed spectrum can be modeled as a linear combination of pure spectra, known as endmembers (Adams et al., 1986; Ramsey and Christensen, 1998). Under ideal conditions, the most accurate fractional estimates can be achieved using the minimum number of endmembers required to account for spectral variability within a mixed pixel (Sabol et al. 1992). Fractional errors occur either where too few endmembers are used, resulting in spectral information not modeled by the existing endmembers; or too many, resulting in incorrect endmember assignment that is used in the model, but not actually present (Roberts et al., 1998). The iterative Multiple Endmember Spectral Mixture Analysis (MESMA) technique can account

for within-class variability and is applied by running numerous models for a pixel and selecting one model based on its ability to meet selection criteria and produce the best fit, typically a minimum RMS (Painter et al. 1998). Selection criteria include fractional constraints (minimum and maximum fraction constrains), maximum allowable blackbody fraction, RMSE constraints and a residual constraint set to remove any model that exceeds a threshold over a range of wavelengths. Using this approach, pixel-scale limits in spectral dimensionality are recognized despite the considerable spectral variability within a scene. The model constraints are variably selectable, whereby MESMA can also be run in an unconstrained mode. Previous studies have found that the flexible MESMA approach resulted in the majority of pixels in an image being modeled with only two-endmember models (Roberts et al. 1998). For example, Powell and Roberts (2008) found that natural landscapes in Brazil required only two-endmember models, disturbed regions required three- and urban areas required four-endmember models.

3.3 Wight Percent Silica (WPS)

To be updated (Hook et al., 2005)

3.5 Sensitivity Analysis

To be updated

4 Surface Mineralogy (SM) Algorithm

The surface mineralogy (SM) algorithm for SBG must rapidly and accurately detect mineral abundances across Earth's low vegetation surfaces (i.e., dunes, volcano, wildland fire scars, arid regions) with a low RMSE. Two main groups of algorithms were tested: SMA and MESMA, based on the widespread usage in the community and previous development and refinement activities.

The testing approach and the results are first described below with the final SM algorithm implementation presented in §4.4.2 and §4.5.

4.1 Test Data Creation

Five simulated OTTER datasets were created from airborne MASTER data using the pre-existing MASTER wavelengths or weighted band averages for the OTTER band center positions that did not align with those of MASTER (Figure 5). The data were also spatially resampled to the planned resolution of OTTER and the atmospheric correction was modified for the performance characteristics (e.g., FPA response) and viewing geometry of OTTER. These simulated data were chosen to test many of the SBG geology higher level data products and therefore include data with known thermal anomalies others with no thermally elevated areas. The latter included compositionally varied targets (e.g., Kelso Dunes, Yosemite National Park) for testing the Surface Mineralogy (SM) product algorithms. However, here they served as null test locations for the ETF algorithm. Both day and night time datasets were utilized.

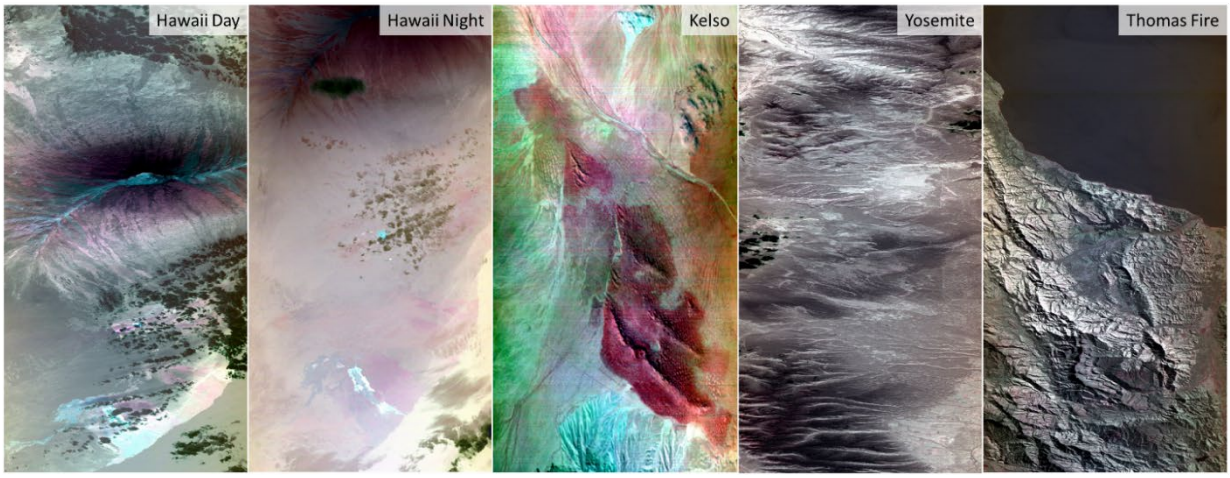

Figure 5: False color image data (11.35, 9.07, 8.32 µm: RGB) of the simulated OTTER data used in the ETF algorithm testing process.

4.2 Algorithm Testing Criteria

Two main previously developed algorithms were considered for testing that utilize an SMA and MESMA approach (Ramsey and Christensen 1998; Roberts et al. 1998). These were chosen based on the availability, accessibility, and high usage across the Earth science community.

4.3 Methodology

4.3.1 Spectral Library Endmember Selection

Nine spectral endmembers were chosen for the SM product (Table 4). These were selected because they are major rock-forming minerals and are generally considered the most abundant on the Earth's surface (*REF*). The focus of the TIR Surface Mineralogy product is on silicate minerals (with two exceptions), all of which have dominate spectral features in the TIR region. Alteration minerals such as oxides and clays are better detected in the VSWIR region and the focus of that SBG sensor.

Table 4: Endmember minerals selected for the SM product spectral library

Mineral Name	Mineral Class	Mineral Group	Chemical Formula	ASU Spectral Library number
Andesine	silicate	feldspar	$(Ca, Na)(Al, Si)_4O_8$	434
Augite	silicate	pyroxene	$(Ca,Na)(Mg,Fe,Al,Ti)(Si,Al)_2O_6$	480
Calcite	carbonate		$CaCO_3$	527
Forsterite	silicate	olivine	Mg_2SiO_4	441
Gypsum	sulfate		$CaSO_4 \cdot 2H_2O$	758
Hornblende	silicate	amphibole	$Ca_2(Mg,Fe,Al)_5(Al,Si)_8O_{22}(OH)_2$	469
Microcline	silicate	feldspar	$KAlSi_3O_8$	490
Muscovite	silicate	mica	$KAl_2(AlSi_3O_{10})(F,OH)_2$	449
Quartz	silicate		SiO_4	1969

The spectral are plotted in Figure 6 at full spectral resolution (2 cm^{-1}) and down sampled to the proposed six band SBG resolution. Importantly, with the addition of the sixth TIR band at 10.3 μm, the spectral diversity of these nine minerals produces distinct spectral shapes in the six-

point spectral ensuring little confusion in mapping these minerals in the SBG data. The addition of the tenth blackbody (ε = 1.0 at all wavelengths) endmember provides a way to account for the discrepancy in spectral depth between the laboratory-measured endmember minerals and that of the image-based data. A blackbody endmember image will be produced, however if normalized out of the total percentage per pixel, the remaining endmember percentages will sum to 100%.

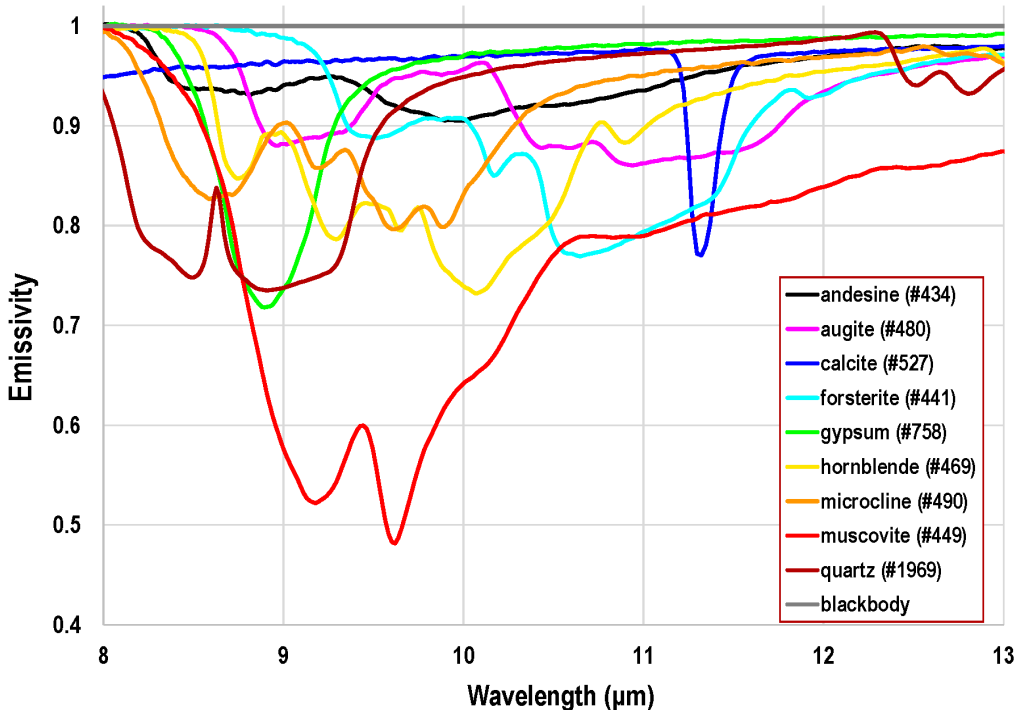

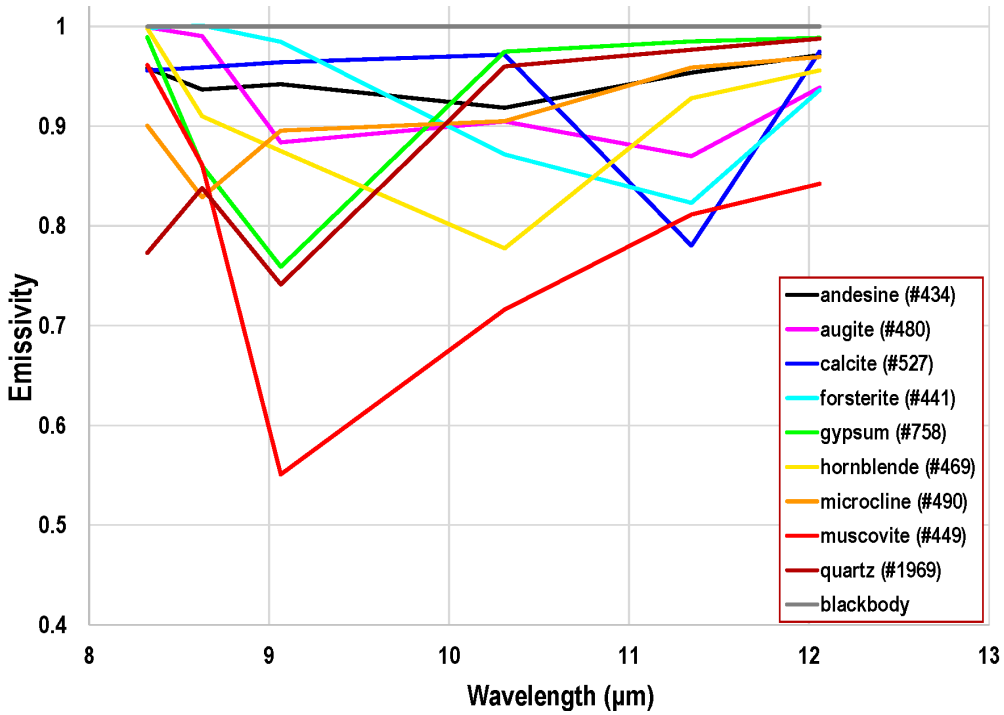

Figure 6: TIR (8.0 – 13.0 µm) spectral emissivity endmembers chosen for testing and eventual implementation of the SM Algorithm. Top: laboratory spectral resolution. Bottom: spectra resampled to the OTTER TIR spectral resolution. Data from: ASU Spectral Library (Christensen et al., 2000).

4.4 SM Algorithm Testing

4.4.1 Subset for Expanded Evaluation

4.4.1.1 Kelso Dunes

The Kelso Dunes are located in the eastern Mojave Desert,California,~95 km west of the California-Arizona border. The rocks that compose the mountain ranges surrounding the dunes range from metamorphosed Proterozoic island-arc remnants, which form much of the southern Kelso Mountains, to Paleozoic metasedimentary rocks that compose the majority of the northern Granite and portions of the Providence Mountains, to Tertiary rhyolite in the Providence Mountains (Jennings, 1961; Bishop, 1963). Also present is the Teutonia batholith, the dominant intrusive rock in the eastern Mojave Desert. It was emplaced throughout later Mesozoic time and ranges compositionally from monzonite to granodiorite (Beckerman et al., 1982). In the vicinity

of the dunes, the batholith is primarily a quartz monzonite (McDonald and McFadden, 1994), weathering to 1 cm grus of alkali feldspar and plagioclase with lesser amounts of quartz.

The Kelso dune field covers more than 100 km^2 and is contained within a topographic basin bounded by the Kelso, Providence, Granite, and Bristol Mountains to the north, east, south, and west, respectively. Earlier studies estimated the dunes to be mature with 70-90% quartz (Sharp, 1966; Paisley et al., 1991); however, later studies using TIR data and detailed field sampling showed the dunes to have a much higher feldspar and lower quartz content indicating a less mature dune field with sand input from local sources (Ramsey et al., 1999).

Daytime TIR airborne data were acquired over the Kelso Dunes region, southern California on September 20, 1999 at 18:47 UTC (10:47 PDT). The algorithms were applied to the emissivity data using five and ten endmembers for the SMA and MESMA approaches, respectively. SMA and MESMA analysis required 6.7 $x10^{-5}$ and 7.4 $x10^{-7}$ seconds per pixel, respectively (Figure 7).

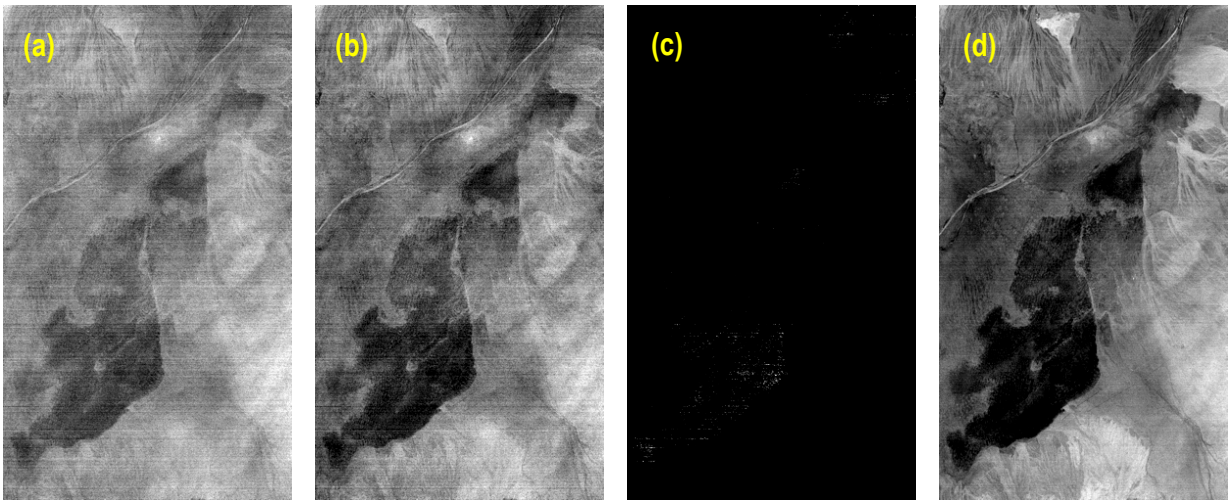

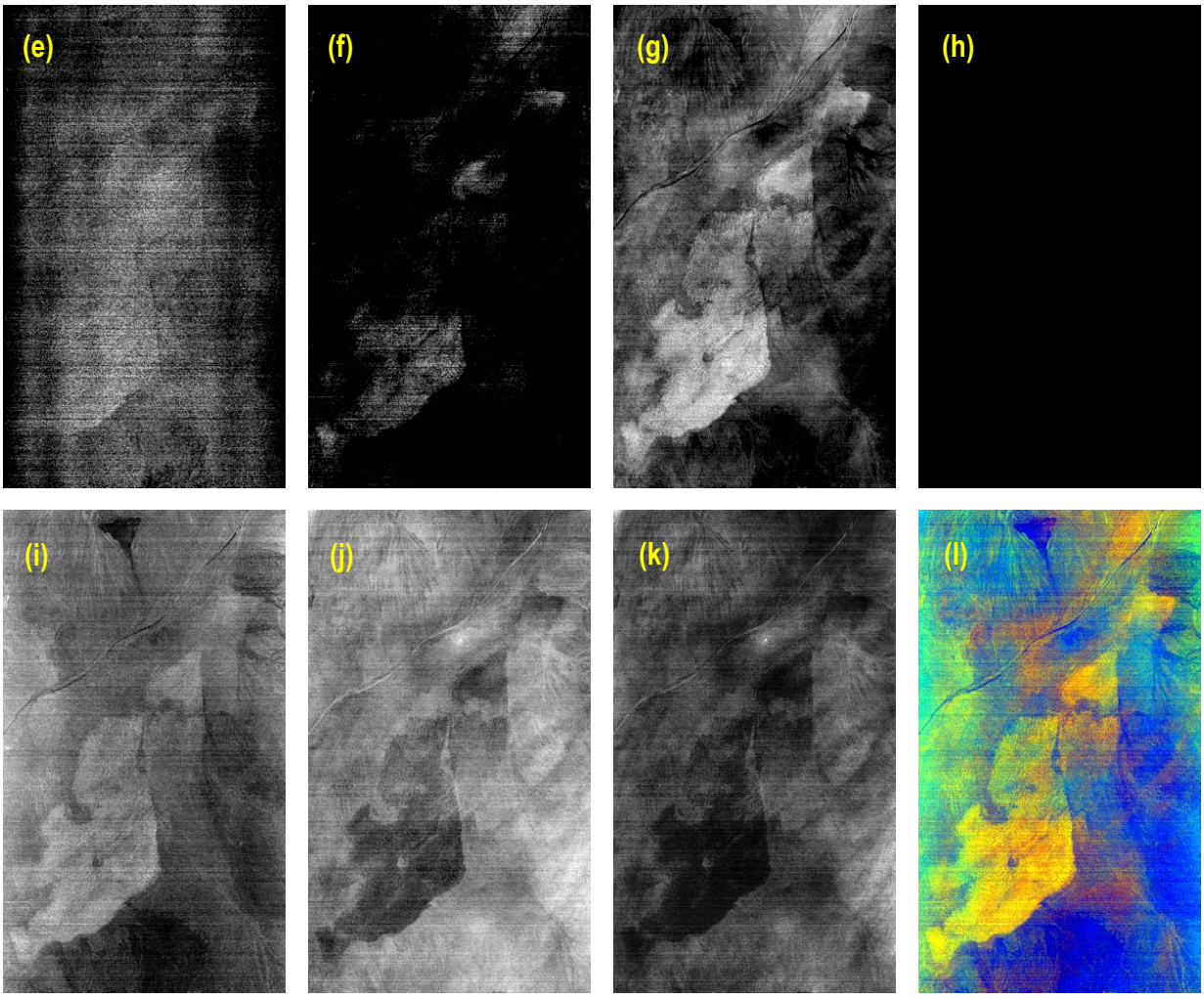

Figure 7: "Fast" MESMA linear deconvolution mineral mapping results using the 10 endmember spectral library (Fig. 6) and the simulated SBG test data for Kelso Dunes, CA. (a) Plagioclase feldspar (andesine), (b) olivine (augite), (c) calcite, (d) pyroxene (forsterite), (e) gypsum, (f) amphibole (hornblende), (g) potassium feldspar (microcline), (h) mica (muscovite), (i) quartz, (j) blackbody, (k) RMS error, (l) color composite of microcline, quartz, and andesine endmembers in R, G, B, respectively.

4.4.2 Final Algorithm Selection

4.5 SBG SM Algorithm Testing

T.B.D. once final algorithm choice is determined.

4.5.1 Data Inputs

T.B.D. once final algorithm choice is determined.

4.5.2 Algorithm Limitations

T.B.D. once final algorithm choice is determined.

4.5.3 SM Workflow

T.B.D. once final algorithm choice is determined.

4.5.4 Implementation Strategy for SBG Mission

T.B.D. once final algorithm choice is determined.

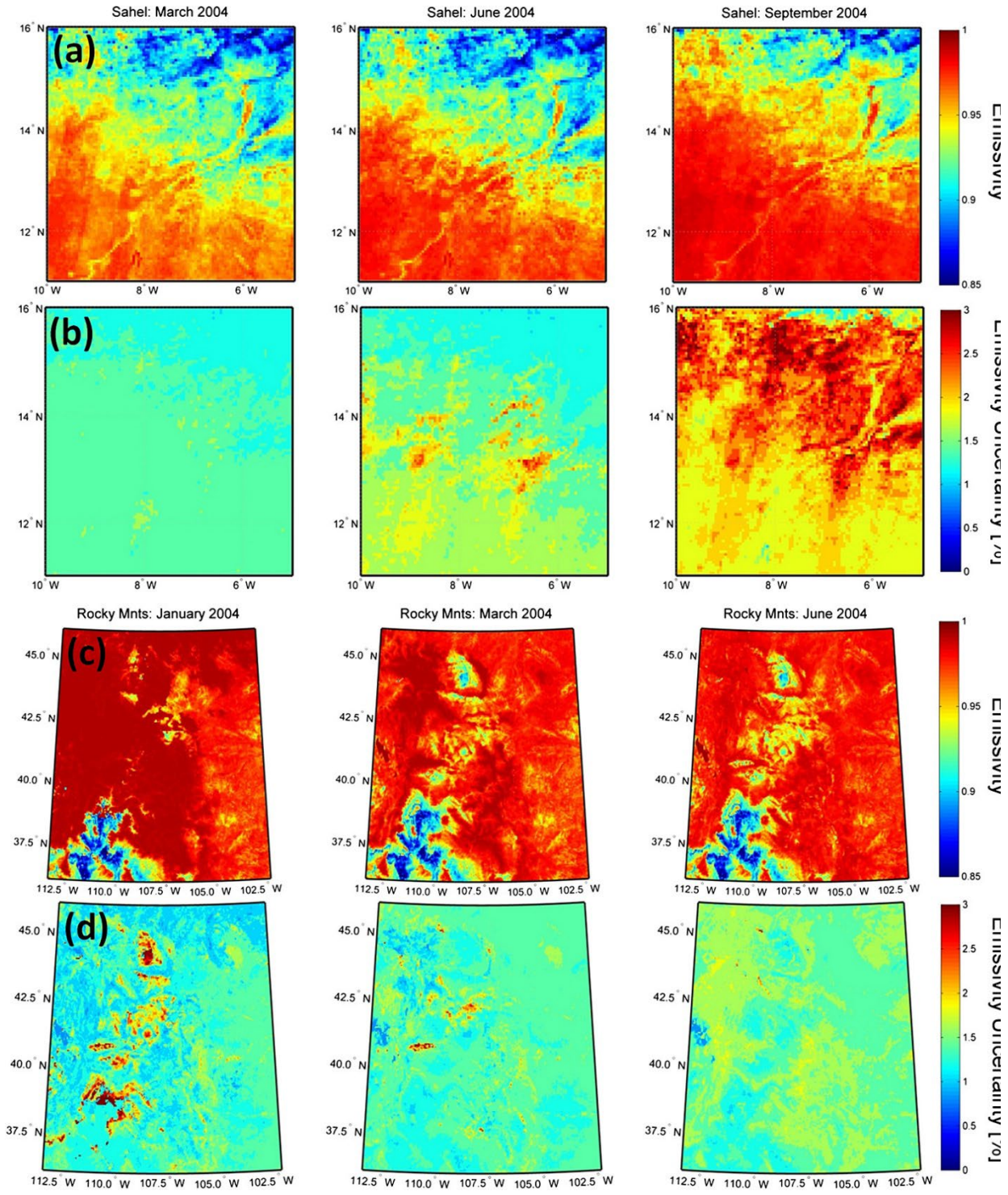

Figure 8: (a) ASTER GEDv4 monthly emissivity showing increasing emissivity due to vegetation green up from summer rainfall over the Sahel, Senegal, from March to September 2004 and (b) corresponding emissivity uncertainty estimate (%). (c) ASTER GEDv4 monthly emissivity showing decreasing emissivity with snowmelt from January to June 2004 over the Rocky Mountains in Colorado and (d) corresponding emissivity uncertainty estimate (%). (Hulley et al., 2015).

4.6 Error Propagation

T.B.D. once final algorithm choice is determined.

5 Uncertainty Analysis

NASA has identified a major need to develop long-term, consistent products valid across multiple missions, with well-defined uncertainty statistics addressing specific Earth-science questions. These products are termed Earth System Data Records (ESDRs).

Completed once final algorithm choice is determined.

6 Quality Control and Diagnostics

T.B.D. once final algorithm choice is determined.

7 Scientific Data Set (SDS) Variables

Table 5. The Scientific Data Sets (SDSs) for the L3 SBG Surface Mineralogy (SM) product

SDS	Long Name	Data type	Units	Valid Range	Fill Value	Scale Factor	Offset
Group	**SDS**						
Amph%	Amphibole Percentage	Int8	%	1-255	0		
Carb%	Carbonate Percentage	Int8	%	1-255	0		
Mica%	Mica Percentage	Int8	%	1-255	0		
Oliv%	Olivine Percentage	Int8	%	1-255	0		
Plag%	Plagioclase Feldspar Percentage	Int8	%	1-255	0		
Kspr%	Potassium Feldspar Percentage	Int8	%	1-255	0		
Pyrx%	Pyroxene Percentage	Int8	%	1-255	0		
Qrtz%	Quartz Percentage	Int8	%	1-255	0		
Gyps%	Gypsum Percentage	Int8	%	1-255	0		
Bb%	Blackbody Percentage	Int8	%	1-255	0		
TIR1-res	TIR Band 1 Residual Error	Float16	n/a	0-65535	0		
TIR2-res	TIR Band 2 Residual Error	Float16	n/a	0-65535	0		
TIR3-res	TIR Band 3 Residual Error	Float16	n/a	0-65535	0		
TIR4-res	TIR Band 4 Residual Error	Float16	n/a	0-65535	0		
TIR5-res	TIR Band 5 Residual Error	Float16	n/a	0-65535	0		
TIR6-res	TIR Band 6 Residual Error	Float16	n/a	0-65535	0		
RMS-err	RMS Error	Float16	n/a	0-65535	0		
WPS	Wt% silica	Float16	%	0-65535	0		
QC	Data Quality	Int8	n/a	1-255	0		

8 Calibration/Validation Plans

8.1 Pre-Launch Algorithm Calibration and Testing

T.B.D. once final algorithm choice is determined.

8.1.1 Expanded Test Dataset

T.B.D. once final algorithm choice is determined.

8.2 Post-Launch Validation Methodology

T.B.D. once final algorithm choice is determined.

8.2.1 Target Sites

T.B.D. once final algorithm choice is determined.

Acknowledgements

The research was carried out at the Jet Propulsion Laboratory, California Institute of Technology, under a contract with the National Aeronautics and Space Administration.

9 References

Adams, J.B., Smith, M.O., Johnson, P.E. (1986). Spectral mixture modeling: A new analysis of rock and soil types at the Viking Lander 1 site. Journal of Geophysical Research: Solid Earth, 91(B8), 8098-8112.

Beckerman, G.M., Robinson, J.P., Anderson, J.L., Frost, E.G., Martin, D.L. (1982). The Teutonia batholith: A large intrusive complex of Jurassic and Cretaceous age in the eastern Mojave Desert, California. Mesozoic-Cenozoic tectonic evolution of the Colorado River region, California, Arizona, and Nevada: San Diego, California, Cordilleran Publishers, 205-220.

Bishop, C.C. (1963). Geologic map of California, needles sheet, scale 1: 250,000. California Division of Mines and Geology Regional Geologic Map Series.

Brown, O., Minnett, P. (1999). MODIS infrared sea surface temperature algorithm. Algorithm Theoretical Basis Document Version 2, Univ. of Miami, Miami, Fla.

Christensen, P.R., Bandfield, J.L., Hamilton, V.E., Howard, D.A., Lane, M.D., Piatek, J.L., ... Stefanov, W.L. (2000). A thermal emission spectral library of rock-forming minerals. Journal of Geophysical Research: Planets, 105(E4), 9735-9739.

Clark, R.N., Swayze, G.A., Wise, R., Livo, K.E., Hoefen, T.M., Kokaly, R.F., Sutley, S.J. (2003). USGS digital spectral library splib06a. US Geological Survey, Open File Report, 3395.

Coll, C., Caselles, V., Galve, J.M., Valor, E., Niclos, R., Sanchez, J.M., Rivas, R. (2005). Ground measurements for the validation of land surface temperatures derived from AATSR and MODIS data. Remote Sensing of Environment, 97, 288-300.

Connelly, D.S., Thompson, D.R., Mahowald, N.M., Li, L., Carmon, N., Okin, G.S., Green, R. O. (2021). The EMIT mission information yield for mineral dust radiative forcing. Remote Sensing of Environment, 258, 112380.

Franke, J., Roberts, D. A., Halligan, K., Menz, G. (2009). Hierarchical multiple endmember spectral mixture analysis (MESMA) of hyperspectral imagery for urban environments. Remote Sensing of Environment, 113(8), 1712-1723.

Gillespie, A. R. (1990). Interpretation of residual images: spectral mixture analysis of AVIRIS images, Owens Valley, California. In Proc. second airborne visible/infrared imaging spectrometer (AVIRIS) workshop (pp. 243-270). Jet Propulsion Laboratory.

Gillespie, A., Rokugawa, S., Matsunaga, T., Cothern, J.S., Hook, S., Kahle, A.B. (1998). A temperature and emissivity separation algorithm for Advanced Spaceborne Thermal Emission and Reflection Radiometer (ASTER) images. IEEE Transactions on Geoscience and Remote Sensing, 36, 1113-1126

Heinz, D. C. (2001). Fully constrained least squares linear spectral mixture analysis method for material quantification in hyperspectral imagery. IEEE transactions on geoscience and remote sensing, 39(3), 529-545.

Helder, D. L., Basnet, B., Morstad, D. L. (2010). Optimized identification of worldwide radiometric pseudo-invariant calibration sites. Canadian Journal of Remote Sensing, 36(5), 527-539.

Hook, S.J., Dmochowski, J.E., Howard, K.A., Rowan, L.C., Karlstrom, K.E., Stock, J. M. (2005). Mapping variations in weight percent silica measured from multispectral thermal infrared

imagery—Examples from the Hiller Mountains, Nevada, USA and Tres Virgenes-La Reforma, Baja California Sur, Mexico. Remote Sensing of Environment, 95(3), 273-289.

Hulley, G.C., Hook, S.J., Abbott, E., Malakar, N., Islam, T., Abrams, M. (2015). The ASTER Global Emissivity Dataset (ASTER GED): Mapping Earth's emissivity at 100 meter spatial scale. Geophysical Research Letters, 42, 7966-7976.

Hulley, G., Baldridge, A. (2013). Validation of thermal infrared (TIR) emissivity spectra using pseudo-invariant sand dune sites. In Thermal Infrared Remote Sensing: Sensors, Methods, Applications (pp. 515-527). Dordrecht: Springer Netherlands.

Jennings, C.W. (1961). Geologic map of California: Kingman sheet, scale 1: 250,000. California Division of Mines and Geology, Sacramento, CA.

McDonald, E., McFadden, L.D., McGill, S.F., Ross, T. M. (1994). Quaternary stratigraphy of the Providence Mountains piedmont and preliminary age estimates and regional stratigraphic correlations of Quaternary deposits in the eastern Mojave Desert, California. Quaternary stratigraphy and dating methods: Understanding geologic processes and landscape evolution in southern California, in McGill, SF, and Ross, TM, eds., Geological investigations of an active margin: Geological Society of America, Cordilleran Section Guidebook, 205-210.

National Academies of Sciences, Engineering, and Medicine (NASEM). (2019). Thriving on our changing planet: A decadal strategy for Earth observation from space. National Academies Press.

Norman, J.M., Becker, F. (1995). Terminology in thermal infrared remote sensing of natural surfaces. Agricultural and Forest Meteorology, 77(3-4), 153-166.

Painter, T.H., Dozier, J., Roberts, D.A., Davis, R.E., Green, R.O. (2003). Retrieval of subpixel snow-covered area and grain size from imaging spectrometer data. Remote Sensing of Environment, 85(1), 64-77.

Paisley, E.C., Lancaster, N., Gaddis, L.R., Greeley, R. (1991). Discrimination of active and inactive sand from remote sensing: Kelso Dunes, Mojave Desert, California. Remote Sensing of Environment, 37(3), 153-166.

Powell, R.L., Roberts, D. A. (2008). Characterizing variability of the urban physical environment for a suite of cities in Rondonia, Brazil. Earth Interactions, 12(13), 1-32.

Prata, A.J. (1994). Land-Surface Temperatures Derived from the Advanced Very High-Resolution Radiometer and the Along-Track Scanning Radiometer .2. Experimental Results and Validation of AVHRR Algorithms. Journal of Geophysical Research-Atmospheres, 99, 13025-13058

Price, J.C. (1984). Land surface temperature measurements from the split window channels of the NOAA 7 Advanced Very High Resolution Radiometer. Journal of Geophysical Research, 89, 7231-7237

Ramsey, M.S., Christensen, P.R., Lancaster, N., Howard, D.A. (1999). Identification of sand sources and transport pathways at the Kelso Dunes, California using thermal infrared remote sensing, Geological Society of America Bulletin, 111, 646-662.

Ramsey, M.S., Christensen, P. R. (1998). Mineral abundance determination: Quantitative deconvolution of thermal emission spectra. Journal of Geophysical Research: Solid Earth, 103(B1), 577-596.

Roberts, D.A., Gardner, M., Church, R., Ustin, S., Scheer, G., Green, R. O. (1998). Mapping chaparral in the Santa Monica Mountains using multiple endmember spectral mixture models. Remote sensing of environment, 65(3), 267-279.

Sabol, D.E., Adams, J.B., Smith, M.O. (1992). Quantitative subpixel spectral detection of targets in multispectral images. Journal of Geophysical Research: Planets, 97(E2), 2659-2672.

Scheidt, S., Lancaster, N., Ramsey, M. (2011). Eolian dynamics and sediment mixing in the Gran Desierto, Mexico, determined from thermal infrared spectroscopy and remote-sensing data. Bulletin, 123(7-8), 1628-1644.

Scheidt, S., Ramsey, M., Lancaster, N. (2010). Determining soil moisture and sediment availability at White Sands Dune Field, New Mexico, from apparent thermal inertia data. Journal of Geophysical Research: Earth Surface, 115(F2).

Schimel, D.S., Poulter, B. (2022, March). The Earth in Living Color-NASA's Surface Biology and Geology Designated Observable. In 2022 IEEE Aerospace Conference (AERO) (pp. 1-6). IEEE.

Sharp, R.P. (1966). Kelso Dunes, Mojave Desert, California. Geological Society of America Bulletin, 77(10), 1045-1074.

Somers, B., Asner, G. P., Tits, L., Coppin, P. (2011). Endmember variability in spectral mixture analysis: A review. Remote Sensing of Environment, 115(7), 1603-1616. Wan, Z.M., & Dozier, J. (1996). A generalized split-window algorithm for retrieving land-surface temperature from space. Ieee Transactions on Geoscience and Remote Sensing, 34, 892-905

Tompkins, S., Mustard, J. F., Pieters, C. M., Forsyth, D. W. (1997). Optimization of endmembers for spectral mixture analysis. Remote Sensing of Environment, 59(3), 472-489.

Wan, Z., Dozier, J. (1996). A generalized split-window algorithm for retrieving land-surface temperature from space. IEEE Transactions on geoscience and remote sensing, 34(4), 892-905.

Yu, Y., Privette, J.L., Pinheiro, A.C. (2008). Evaluation of split-window land surface temperature algorithms for generating climate data records. Ieee Transactions on Geoscience and Remote Sensing, 46, 179-192